Preliminary Analysis of an Oscillating Surge Wave Energy Converter with Controlled Geometry

Preprint

Nathan Tom, Michael Lawson, Yi-Hsiang Yu, and Alan Wright
National Renewable Energy Laboratory

To be presented at the European Wave and Tidal Energy Conference
Nantes, France
September 6–11, 2015

NREL is a national laboratory of the U.S. Department of Energy
Office of Energy Efficiency & Renewable Energy
Operated by the Alliance for Sustainable Energy, LLC

This report is available at no cost from the National Renewable Energy Laboratory (NREL) at www.nrel.gov/publications.

Conference Paper
NREL/CP-5000-64545
September 2015

Contract No. DE-AC36-08GO28308

NOTICE

The submitted manuscript has been offered by an employee of the Alliance for Sustainable Energy, LLC (Alliance), a contractor of the US Government under Contract No. DE-AC36-08GO28308. Accordingly, the US Government and Alliance retain a nonexclusive royalty-free license to publish or reproduce the published form of this contribution, or allow others to do so, for US Government purposes.

This report was prepared as an account of work sponsored by an agency of the United States government. Neither the United States government nor any agency thereof, nor any of their employees, makes any warranty, express or implied, or assumes any legal liability or responsibility for the accuracy, completeness, or usefulness of any information, apparatus, product, or process disclosed, or represents that its use would not infringe privately owned rights. Reference herein to any specific commercial product, process, or service by trade name, trademark, manufacturer, or otherwise does not necessarily constitute or imply its endorsement, recommendation, or favoring by the United States government or any agency thereof. The views and opinions of authors expressed herein do not necessarily state or reflect those of the United States government or any agency thereof.

This report is available at no cost from the National Renewable Energy Laboratory (NREL) at www.nrel.gov/publications.

Available electronically at SciTech Connect http:/www.osti.gov/scitech

Available for a processing fee to U.S. Department of Energy and its contractors, in paper, from:

U.S. Department of Energy
Office of Scientific and Technical Information
P.O. Box 62
Oak Ridge, TN 37831-0062
OSTI http://www.osti.gov
Phone: 865.576.8401
Fax: 865.576.5728
Email: reports@osti.gov

Available for sale to the public, in paper, from:

U.S. Department of Commerce
National Technical Information Service
5301 Shawnee Road
Alexandria, VA 22312
NTIS http://www.ntis.gov
Phone: 800.553.6847 or 703.605.6000
Fax: 703.605.6900
Email: orders@ntis.gov

Cover Photos by Dennis Schroeder: (left to right) NREL 26173, NREL 18302, NREL 19758, NREL 29642, NREL 19795.

NREL prints on paper that contains recycled content.

Preliminary Analysis of an Oscillating Surge Wave Energy Converter with Controlled Geometry

Nathan Tom[1], Michael Lawson[2], Yi-Hsiang Yu[3], Alan Wright[4]

National Wind Technology Center, National Renewable Energy Laboratory
15013 Denver West Parkway, Golden, Colorado USA

[1]nathan.tom@nrel.gov, [2]michael.lawson@nrel.gov, [3]yi-hsiang.yu@nrel.gov, [4]alan.wright@nrel.gov

***Abstract*— The aim of this paper is to present a novel wave energy converter device concept that is being developed at the National Renewable Energy Laboratory. The proposed concept combines an oscillating surge wave energy converter with active control surfaces. These active control surfaces allow for the device geometry to be altered, which leads to changes in the hydrodynamic properties. The device geometry will be controlled on a sea state time scale and combined with wave-to-wave power-take-off control to maximize power capture, increase capacity factor, and reduce design loads. The paper begins with a traditional linear frequency domain analysis of the device performance. Performance sensitivity to foil pitch angle, the number of activated foils, and foil cross section geometry is presented to illustrate the current design decisions; however, it is understood from previous studies that modeling of current oscillating wave energy converter designs requires the consideration of nonlinear hydrodynamics and viscous drag forces. In response, a nonlinear model is presented that highlights the shortcomings of the linear frequency domain analysis and increases the precision in predicted performance.**

***Keywords*— Wave energy converter (WEC), active geometry, oscillating surge WEC, time-varying parameters, load shedding**

I. Introduction

During the past decade, the marine and hydrokinetic energy sector has experienced a resurgence in the funding and manpower allocated towards research and development. As a whole, the field of wave energy continues to host a wide diversity of technologies ranging in scale from concept to prototype. This situation highlights the need for a structured innovative approach to the development of wave energy converters (WECs) in hopes of achieving an optimal convergence in overall design and operation [1]. Recent studies on WEC system designs have shown that the development of advanced control methods that actively tune device performance to maximize energy generation in operational conditions, while minimizing hydrodynamic loading in extreme sea states, is a necessary step in advancing wave energy technologies towards commercial viability [2].

This paper attempts to address such concerns by proposing a new device concept that combines an oscillating surge wave energy converter (OSWEC) with active control surfaces [3][4]. The control surfaces can be thought of as being similar to air foils where it is hoped to modify and apply the controller designs [5] developed at the National Renewable Energy Laboratory (NREL) for wind turbine control.

The development of nearshore oscillating surge wave energy devices has so far been led by Aquamarine Power (Oyster), AW-Energy Oy (WAVEROLLER), and Resolute Marine Energy [6]. In addition, Langlee Wave Power [7] is currently developing a floating dual-flap OSWEC; however, all of these designs consist of a fixed geometrical body that relies on control of the power-take-off (PTO) system to further optimize power absorption.

Previous studies have shown that the general OSWEC design experiences large hydrodynamic loads that drive the structural design and material costs [8]. The novelty of the proposed design is the ability to alter the geometry normal to the particle velocity thereby reducing hydrodynamic loading. Point absorbers are generally narrow banded with high extraction efficiencies only around a small frequency range about its resonance. Flocard and Finnigan [9] did investigate the ability to tune the resonance period of a pitching WEC by altering the devices rotational inertia by shifting the internal mass distribution. A device with a controllable geometry would not only be able to shed loads, but also tune the hydrodynamic characteristics to match the resonance period of the device with the peak period of the sea state and broaden the effective operating range. Furthermore, the ability to shed loads allows the device to continue operating in larger sea states where amplitude or structural loading constraints would force current designs to switch into survival mode.

After the device concept is fully introduced, evaluation of the performance begins with the traditional linear frequency domain analysis. To describe the design evolution, we present the performance sensitivity to foil pitch angle, foil cross section, and number of activated foils; however, current OSWEC designs require considerations for nonlinear hydrodynamics and viscous drag forces [10]. As a result, a nonlinear model was constructed while placing constraints on the pitch motion and PTO torque. The paper ends with a linearization of the quadratic damping from the Lorentz theorem to be used in the described spectral analysis. The linearization allows for the construction of a nonlinear optimization problem that can be solved while incorporating device-specific constraints.

II. Wave Characteristics

The hydrodynamic properties of the OSWEC and propagating power available will be affected by the water depth, h. From linear potential theory, the incident wave potential, ϕ_I, for a right propagating wave is given by:

This report is available at no cost from the National Renewable Energy Laboratory (NREL) at www.nrel.gov/publications.

$$\phi_I = \Re\left\{\frac{igA}{\sigma}\frac{\cosh kz}{\cosh kh}e^{(\sigma t - k(x\cos\beta + y\sin\beta))}\right\} \quad , \qquad (1)$$

where σ is the wave angular frequency, g is gravitational acceleration, k is the wave number, A is the wave amplitude, β is the wave heading measured counter clockwise from the positive x-axis, and i is the imaginary unit ($i=\sqrt{-1}$). Because of the combined free surface boundary condition:

$$\frac{\partial^2 \phi_I}{\partial t^2} + g\frac{\partial \phi_I}{\partial z} = 0 \quad , \qquad (2)$$

the relationship between the wave number and the wave angular frequency is given by the dispersion relation:

$$\sigma^2 = gk\tanh kh \quad , \qquad (3)$$

where the solution of Eqn. (3) can be found in Fig. 1.

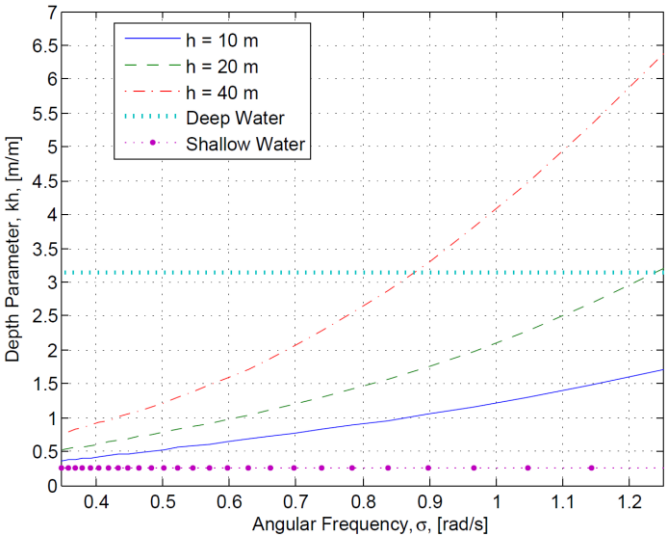

Fig. 1: Depth parameter versus wave angular frequency.

The time-averaged power (TAP) per unit width, P_w, contained within a propagating wave can be shown to equal:

$$P_w = \frac{1}{2}\rho g V_g A^2 \quad , \qquad (4)$$

$$V_g = \frac{1}{2}\sqrt{\frac{g}{k}}\tanh kh\left[1 + \frac{2kh}{\sinh 2kh}\right] \quad , \qquad (5)$$

where ρ is the fluid density and V_g is the group velocity. A plot of power versus wave angular frequency is show in Fig. 2, in which shorter wavelengths will have greater power in shallow water, whereas in deep water longer wavelengths contain significantly more power. Equation (4) assumes the waves propagate along a constant water depth, thus deployment along sloped seabeds should yield reduced extractable power as a result of reflection and frictional losses.

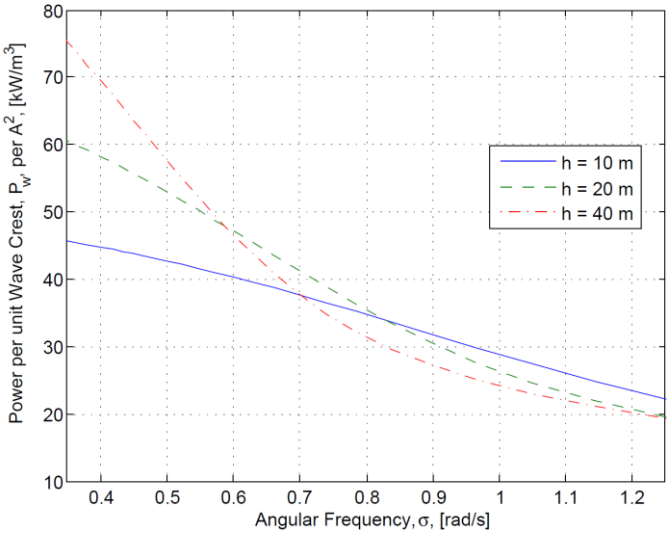

Fig. 2: Wave propagating power versus wave angular frequency.

III. Design Concept

Large hydrodynamic loads are typical for most current OSWEC designs. The added moment of inertia, which arises from radiation effects, can shift the resonance period of the device outside the wave range of 5–20 s. In addition, without active PTO control measures the optimum conditions for power extraction will be difficult to maintain, especially in irregular waves. Therefore, we believe employing active-controllable geometries will allow for greater power optimization and load shedding for continued operation in larger sea states.

A conceptual depiction of the device under investigation is shown in Fig. 3. The general shape of the OSWEC design is a simple flat plate, but the concept under development aims to replace the main body by a set of identical actuated flaps. The flaps will be allowed to pitch freely about their center of rotation with the flap pitch angle, φ, measured positive clockwise from the radial axis of the body as shown in Fig. 4.

The geometric shape of the OSWEC will be allowed to change; however, the mass will be assumed to be evenly distributed throughout the device and the moment of inertia will remain constant and is given by:

$$I_{55} = \frac{1}{3}mH^2 = \frac{1}{3}\rho_m \forall H^2 \quad , \qquad (6)$$

where I_{55} is the moment of inertia about the origin, m is the mass of the OSWEC, H is the height of the OSWEC, ρ_m is the mass density of the OSWEC, and $\forall$ is the displaced volume of the OSWEC. For this study the mass density was set to ½ρ to act as the baseline case.

This report is available at no cost from the National Renewable Energy Laboratory (NREL) at www.nrel.gov/publications.

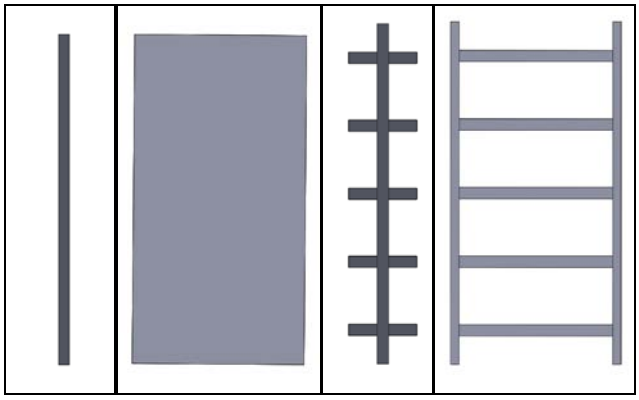

Fig. 3: Conceptual depiction of OSWEC with active geometry. Side views can be found in the first and third images, whereas front views correspond to the second and fourth images.

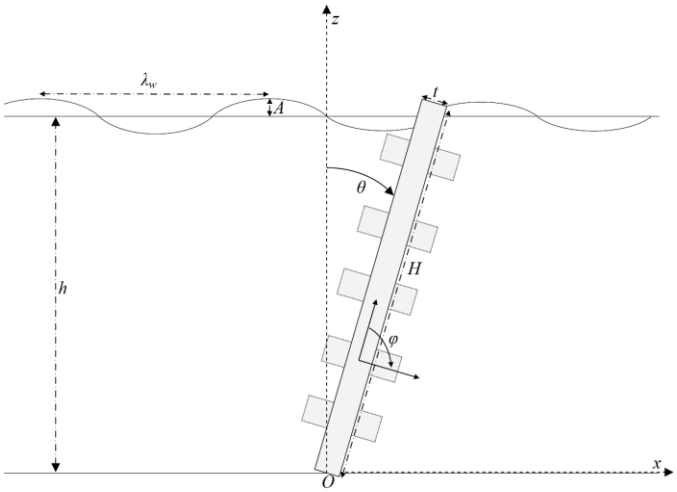

Fig. 4: Schematic of physical system under investigation.

TABLE I
GEOMETRIC PROPERTIES FOR PRELIMINARY HYDRODYNAMIC MODELING

Description	Variable	Unit
Water Depth	h	10 m
OSWEC Height	H	10 m
OSWEC Thickness	t	1/3 m
OSWEC Width	w	5 m
Number of Identical Flaps	n	5
Flap Height	H_f	2 m
Flap Width	w_f	4.5 m
Flap Thickness	t_f	1/3 m
Side Support Height	H_s	10 m
Side Support Thickness	t_s	1/3 m
Side Support Width	w_s	1/4 m

The primary dimensions used in this study, found in Table I, are significantly smaller than other designs approximately 1/4 the width and thickness used by Clabby et al. [11]. The authors of the present work acknowledge that the design can assist in tuning the device's hydrodynamic properties, but it will add loading and bending stress concentrations in the flaps, which will require a reduction in the overall width of the device. This issue is currently being investigated and will ultimately determine if the design is feasible; however, this paper will focus on the hydrodynamic performance.

A. Linear Hydrodynamic Coefficients

The first step in the study of the proposed OSWEC device was examination of the hydrodynamic coefficients for several flap pitch angles, presented in Fig. 5–Fig. 7. The hydrodynamic coefficients were obtained from WAMIT version 7.0 [12]. As expected, when the flap pitch angle is set to zero ($\varphi = 0$) the added moment of inertia dominates and is 25 times the mass moment of inertia. Pitching the flaps to 45 degrees drops the added moment of inertia by a factor of 4; at 90 degrees there is a drop of a factor of 25. Because the mass and restoring moment are not affected by foil pitch angle, the resonance period will increase as the flaps are opened. The wave-exciting force exhibits a similar trend in magnitude; however, for a pitch angle of 45 degrees the phase deviates from 0 and 90 degrees because there is a significant contribution from the real component that arises from the difference in the pressure distribution along the x-axis as the flap is rotated.

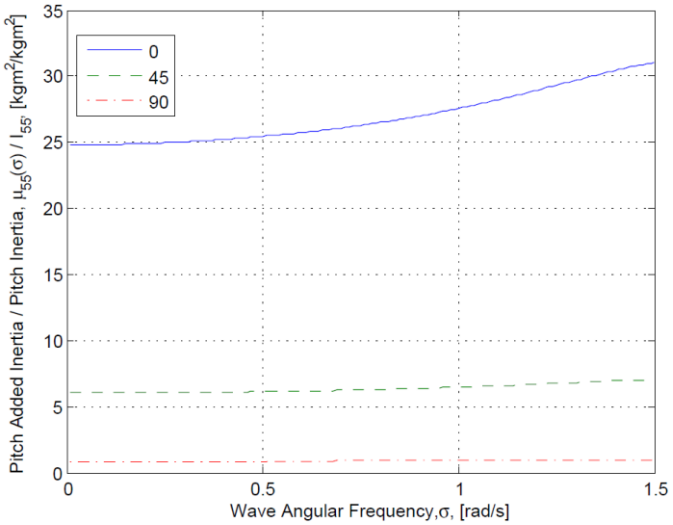

Fig. 5: Ratio of pitch-added moment of inertia to pitch mass inertia for three pitch angles.

IV. EQUATION OF MOTION

It is common practice to calculate the response amplitude operator (RAO) to access the performance of a WEC. For an incident wave described by:

$$\eta(x,t) = \Re\left\{-\frac{1}{g}\frac{\partial \phi_I}{\partial t}\bigg|_{z=h}\right\} = \Re\left\{Ae^{i(\sigma t - kx)}\right\} \quad , \tag{7}$$

where η is the wave elevation, the time-harmonic response of the floating body, in the *j-th* direction, is given by:

$$\zeta_j(t) = \Re\left\{\xi_j e^{i\sigma t}\right\} \quad , \tag{8}$$

This report is available at no cost from the National Renewable Energy Laboratory (NREL) at www.nrel.gov/publications.

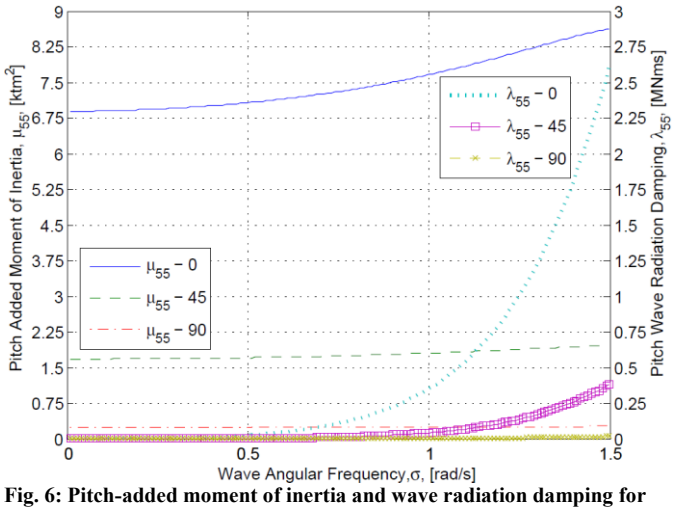

Fig. 6: Pitch-added moment of inertia and wave radiation damping for three pitch angles.

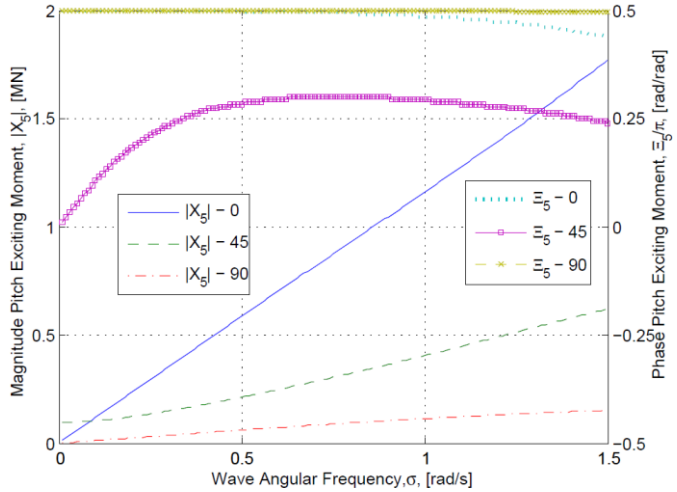

Fig. 7: Magnitude and phase of the wave-exciting force for three pitch angles.

where ξ_j is the complex amplitude of motion for the *j-th* direction. The resulting harmonic motion when allowing for six degrees of freedom can be described by the following coupled system of linear differential equations:

$$\sum_{j=1}^{6}\left[C_{ij}-\sigma^2\left(I_{ij}+\mu_{ij}\right)+i\sigma\lambda_{ij}\right]\xi_j=F_i \quad , \tag{9}$$

where I_{ij} is the generalized inertia matrix, μ_{ij} is the added mass matrix, λ_{ij} is the wave damping matrix, C_{ij} is the restoring matrix, and F_i is the complex amplitude of the wave-exciting force.

B. Linear One Degree of Freedom

As shown in Fig. 4, the OSWEC will pitch about the origin, *O*, which is fixed to the seabed. The other five modes of motion will be constrained and the one degree of freedom pitch equation of motion is given by:

$$\frac{\xi_5}{A}=\frac{X_5}{[C_{55}-\sigma^2(I_{55}+\mu_{55})]+i\sigma[\lambda_{55}+B_g]}, \tag{10}$$

where B_g denotes the linear PTO damping coefficient required for power extraction and X_5 is the complex wave exciting force per unit wave amplitude ($F_5=AX_5$). The instantaneous power absorbed by the PTO is calculated from:

$$\frac{P}{A^2}=\frac{B_g}{A^2}\dot{\zeta}_5^2=B_g\sigma^2\left|\frac{\xi_5}{A}\right|^2\sin^2\left(\sigma t+\Theta\right) \quad , \tag{11}$$

where $|\cdot|$ denotes the magnitude and Θ is the phase of pitch motion. Because the current analysis is in the frequency domain, it is more appropriate to report the time-averaged power (TAP) absorbed by the PTO system, which is calculated as follows:

$$\begin{aligned}\frac{P_{TAP}}{A^2}&=\frac{1}{T}\int_0^T B_g\sigma^2\left|\frac{\xi_5}{A}\right|^2\sin^2\left(\sigma t+\Theta\right)dt\\&=\frac{1}{2}B_g\sigma^2\left|\frac{\xi_5}{A}\right|^2 \quad ,\end{aligned} \tag{12}$$

where T is the wave period. Equation (10) can be inserted into Eqn. (12) allowing for the optimal PTO damping at each wave frequency to be calculated. This results in the following expression:

$$\frac{B_g(\sigma)}{\lambda_{55}(\sigma)}=\sqrt{1+\left(\frac{C_{55}-\sigma^2\left(I_{55}+\mu_{55}(\sigma)\right)}{\sigma\lambda_{55}(\sigma)}\right)^2} \quad , \tag{13}$$

where at resonance $B_g = \lambda_{55}$, which is consistent with the well-known results from [13]. However, Eqn. (13) does not take into account physical constraints that can arise in the final design, which often lead to unrealistic amplitudes of motion that invalidate the linear assumption [14].

1) *Restoring Coefficient*: A hydrostatic restoring moment is present if the OSWEC is positively buoyant $\left(\rho\forall>\rho_m\forall\right)$ and is calculated from:

$$m_h(t)=-\left(\rho\forall r_b-mr_g\right)g\sin\theta \quad , \tag{14}$$

where r_g is the center of gravity, r_b is the center of buoyancy, and m is the mass of the OSWEC. The previous equation can be linearized by assuming small amplitude motion and approximating $\sin\theta \approx \theta$. For this study the mass distribution is assumed uniform; thus $r_g = r_b = H/2$.

This report is available at no cost from the National Renewable Energy Laboratory (NREL) at www.nrel.gov/publications.

The performance results without motion constraints are shown in Fig. 8–Fig. 10. The results show three distinct peaks corresponding to the shifting resonance frequency as the foils are opened. The amplitude of pitch motion per wave slope is greatest for the closed configuration; however, the frequency of oscillation is significantly reduced, leading to comparable energy production. These results indicate that device performance can be tuned over a wide operating range.

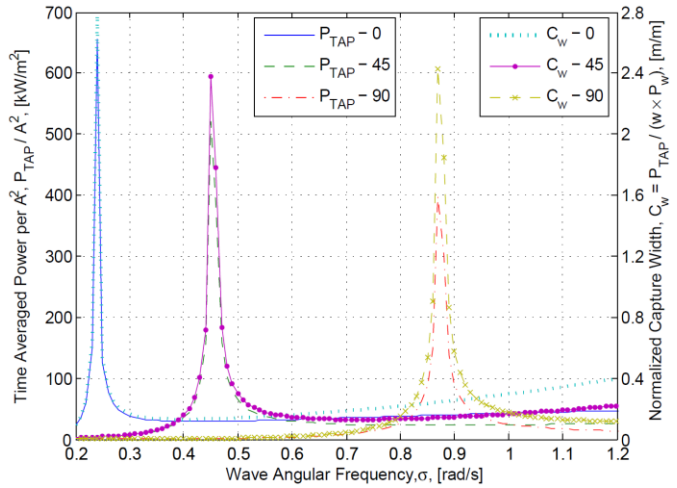

Fig. 8: Optimum time-averaged power and nondimensional capture width for three pitch angles.

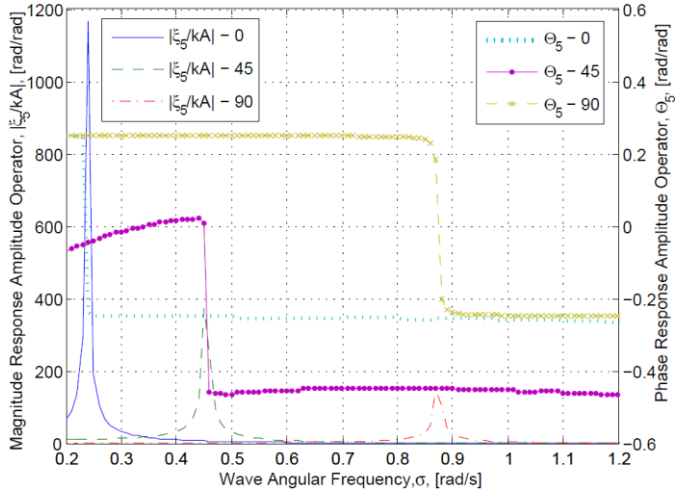

Fig. 9: Unconstrained RAO magnitude and phase with the PTO damping obtained from Eqn. (13) for three pitch angles.

C. Constrained Motion and PTO Power Capacity

As in the previous section, the optimal conditions for power absorption require unconstrained motion and a properly sized PTO; however, in practice, physical limitations such as a hydraulic stroke length will constrain the device's maximum amplitude of motion. Furthermore, as shown in Fig. 10, the optimum performance of the closed flap configuration requires a PTO system that can deliver a linear damping coefficient that is nearly 20 times that of the fully open configuration when operating in the high-frequency regime. Still, both open flap conditions only require a maximum PTO rotational damping of 2 MN.m.s. To address these concerns, the PTO damping was iterated to limit the magnitude of Eqn. (10) to one with an upper limit of 2 MN.m.s. These constraints cause a dramatic reduction in power production and motion as shown in Fig. 11 and Fig. 12, though proper device geometry and PTO configuration can provide a minimum of 25 kW/m^2 over the operating frequency range. The upper limit on the PTO only affects the fully closed geometry and provides only a small frequency window where it was not fixed at the upper limit. The PTO damping also experiences a hump about each resonance period that is a result of the motion constraint as shown in Fig. 13.

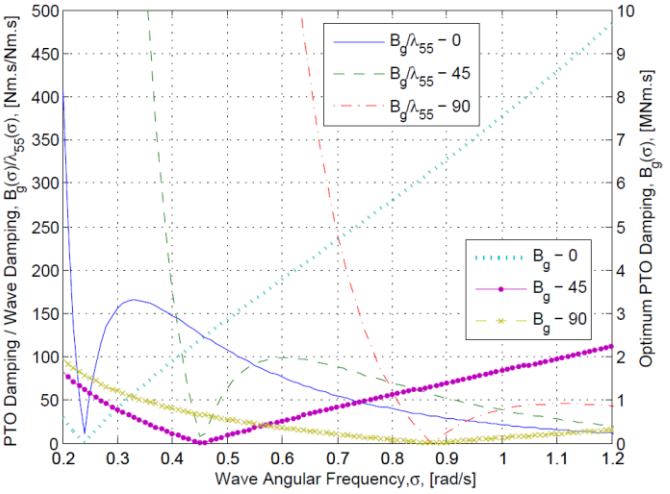

Fig. 10: Unconstrained optimum PTO damping and its ratio with wave damping for three pitch angles.

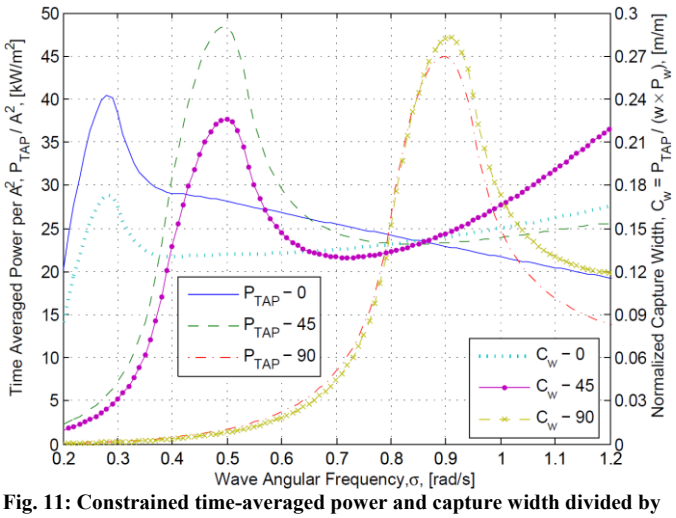

Fig. 11: Constrained time-averaged power and capture width divided by device width for three pitch angles.

V. Foil Cross Section

It is anticipated that the rectangular cross section of the flaps will generate a large amount of vortex shedding caused by the sharp edges [15]. A more streamlined shape will be desired to prevent wave power from being dissipated in eddies rather than being absorbed by the PTO; however, because this is a viscous phenomenon, the effect on power performance cannot be obtained from WAMIT. An attempt to model the viscous contribution will be presented in Section VII and the results in this section will be obtained from WAMIT coefficients.

This report is available at no cost from the National Renewable Energy Laboratory (NREL) at www.nrel.gov/publications.

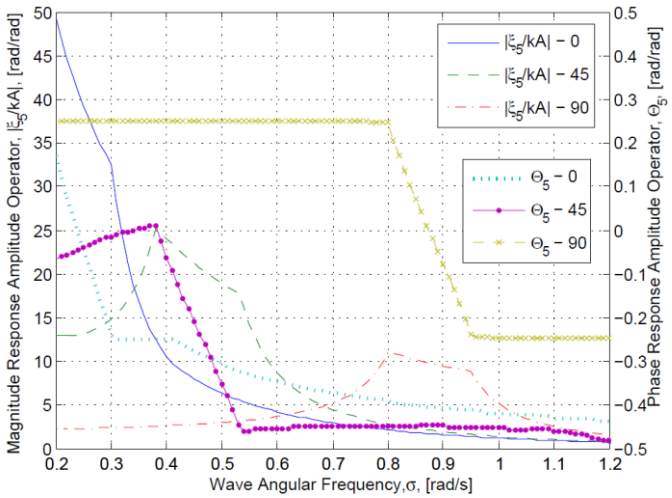

Fig. 12: Constrained RAO magnitude and phase for three pitch angles.

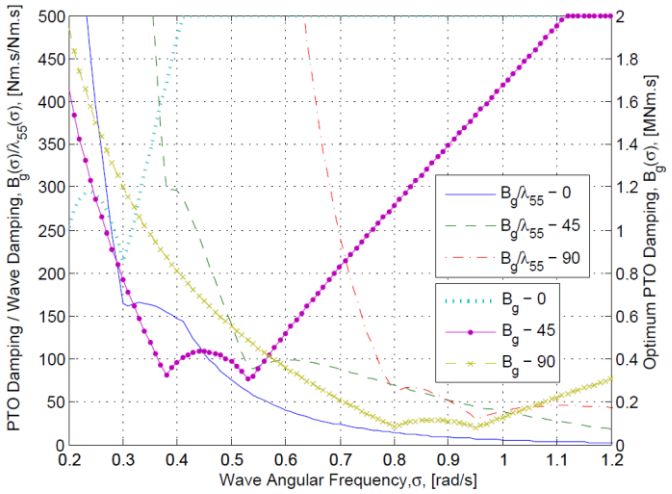

Fig. 13: Constrained PTO damping and its ratio with wave damping for three pitch angles.

For now, an elliptical cross section was chosen with a semimajor axis, *a*, of 1 m and a semiminor axis, *b*, of 1/6 m. The change in cross section will lead to a decrease in the flap displaced volume by approximately 20%. The same constraints on the RAO and PTO rotational damping were applied, and the results are plotted in Fig. 14. The most significant result from the comparison is the nearly 40% drop in time-averaged absorbed power. Yet, to account for the decrease in displaced volume, the time-averaged power was divided by the amplitude of the wave exciting force, which provided comparable results. The change in cross section cut the wave damping by more than 50%, added moment of inertia by 30%, and the wave-exciting force magnitude by 40% as plotted in Fig. 15.

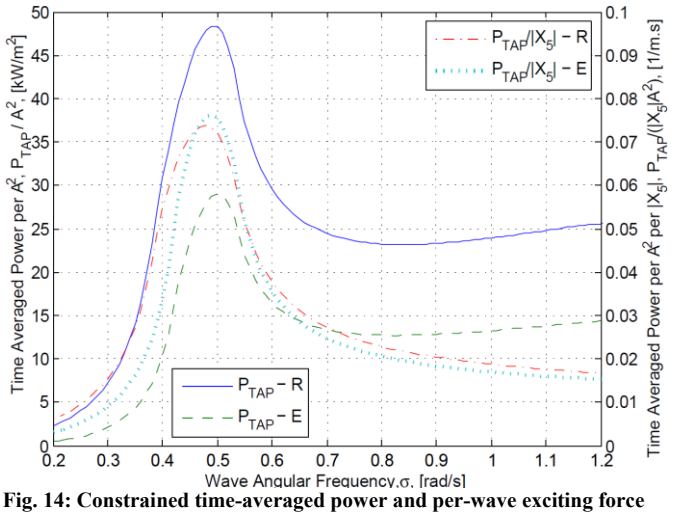

Fig. 14: Constrained time-averaged power and per-wave exciting force amplitude for two flap cross sections.

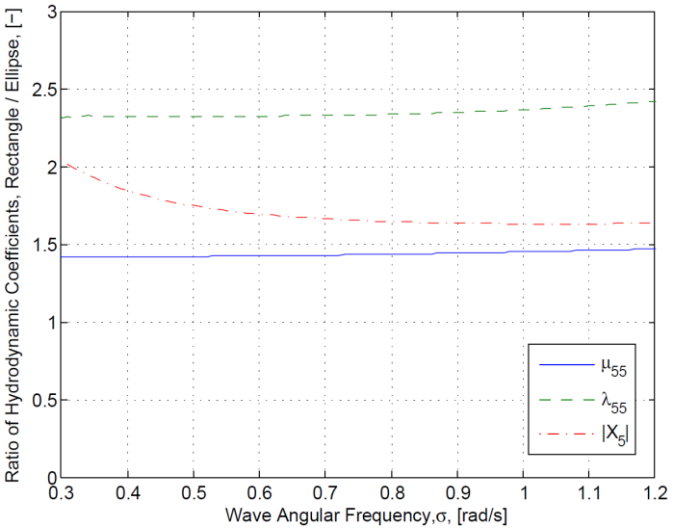

Fig. 15: Ratio of hydrodynamic coefficients for the two cross sections.

VI. Number of Actuated Flaps

In the previous sections, the flaps were actuated in synchronization; however, a simpler control of the geometry may be to open the flaps independently. This would allow for configurations in which the top flap or top two flaps were both pitched to 90 degrees as depicted in Fig. 16. It would not be unexpected to see five resonance peaks accounting for each additional flap opened, which is confirmed in Fig. 17. The simple control allows the device performance to be maximized over the range of 7–16-s wave periods, in which an average value of 40 kW/m^2 is obtainable. Furthermore, as the flaps are opened the structural loading on the device is reduced which will allow for loading constraints to be maintained and peak loads to be reduced if an adequate wave prediction methodology is implemented.

The results from this section also suggest that the fifth (bottom) flap should have little influence on the device performance. As seen in Fig. 17, there is only a small frequency range in which greater power is absorbed when compared to the four-flap configuration. Therefore, it is

This report is available at no cost from the National Renewable Energy Laboratory (NREL) at www.nrel.gov/publications.

expected that the fifth flap be fixed under normal operation. In extreme sea conditions, the fifth flap can be feathered to further reduce loading; however it will likely be more beneficial to permanently fix the flap to add structural rigidity and eliminate additional rotational actuators, thereby reducing the overall complexity of the design.

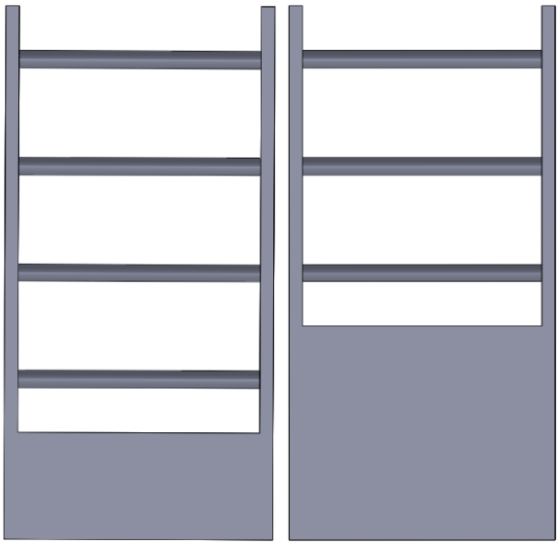

Fig. 16: Solidworks model of two configurations (left: four flaps open and right: three flaps open).

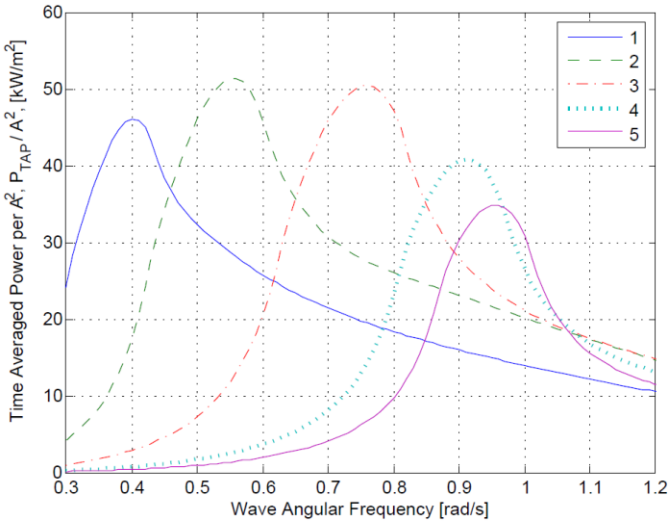

Fig. 17: Time-averaged power for five geometric configurations. The legend indicates the number of flaps fully open, starting from the topmost. PTO damping values were taken from Eqn. (13) with a 0.75 MN.m.s limit.

VII. Viscous Drag

The previous analysis has been completed under the inviscid assumption. This generalization often leads to significant overprediction in device motion and absorbed power. The first attempt at modeling the viscous drag moment begins with Morison's equation [16]:

$$f_d(t) = -\frac{1}{2}\rho C_D(r,\varphi) A_p(r,\varphi) r\dot{\theta}(t)\left|r\dot{\theta}(t)\right| \quad , \tag{15}$$

where f_d is the drag force and C_D is the drag coefficient which is a function of pitch angle and potentially of the radial position, A_p is the projected area of the flap normal to the rotational velocity of the OSWEC, $|\cdot|$ denotes the absolute value, and r denotes the position of the drag element along the radial axis. The moment generated by taking a differential slice of the OSWEC along the *xy*-plane is given by:

$$dM_d(t,\varphi) = -\frac{1}{2}\rho C_D w_f \dot{\theta}(t)\left|\dot{\theta}(t)\right| r^3 dr \quad , \tag{16}$$

where M_D is the drag-induced moment and dr is the differential unit along the radial axis. To obtain the total drag moment, Eqn. (16) must be integrated over the height of the OSWEC:

$$M_d(t,\varphi) = -\frac{1}{2}\rho C_D w_f \dot{\theta}(t)\left|\dot{\theta}(t)\right| \int_0^H r^3 dr \quad . \tag{17}$$

Equation (17) can be integrated directly if the flaps are closed; however, as the flaps are pitched the projected area will need to be adjusted. The change in projected area with flap pitch angle will be modeled as:

$$A_P(\varphi) = 2w_f\left(a\left|\cos\varphi\right| + b\left|\sin\varphi\right|\right) \quad , \tag{18}$$

with the bounds of integration in Eqn. (17) set to:

$$r = r_{ci} \pm \left(a\left|\cos\varphi\right| + b\left|\sin\varphi\right|\right) \quad , \tag{19}$$

where r_{ci} is the radial position of the center of rotation of the *i-th* flap. The total drag moment is the summation over the total number of flaps:

$$M_d(t,\varphi) = -\sum_{i=1}^{N} M_{di} \quad , \tag{20}$$

$$M_{di} = \frac{1}{8}\rho w_f C_D(\varphi)\dot{\theta}(t)\left|\dot{\theta}(t)\right| r^4 \Big|_{r_{ci}-\left(a\left|\cos\varphi\right|+b\left|\sin\varphi\right|\right)}^{r_{ci}+\left(a\left|\cos\varphi\right|+b\left|\sin\varphi\right|\right)} . \tag{21}$$

The drag coefficient was assumed to be constant over the foil. The difficulty in modeling is the appropriate choice of $C_D(\varphi)$ as the projected area is reduced, at most, by a factor of 1/6. For this analysis the following drag coefficients were used: $C_D(0) = 1.9$ and $C_D(90) = 0.1$.

This report is available at no cost from the National Renewable Energy Laboratory (NREL) at www.nrel.gov/publications.

Often the rotational velocity, in Eqn. (17), is subtracted by the undisturbed fluid orbital velocity, as described in Babarit et al. [17]. A nonlinear time domain model was constructed to ascertain the effect of the modelling approximation. Results showed minor differences and will not be discussed further in this preliminary analysis.

The nonlinear time domain model was used to evaluate performance sensitivity to wave height. The viscous drag reduced the power capture efficiency by up to 60% for the largest wave amplitude, Fig. 18. The absorbed power has local maximums for each configuration; however, the two-flap geometry is the most robust over the frequency range as plotted in Fig. 19.

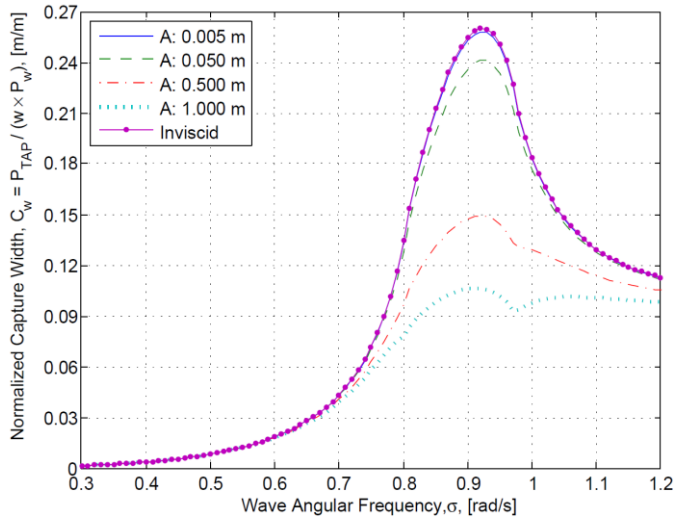

Fig. 18: Variation of nondimensional capture width with wave amplitude for the configuration with four flaps open. PTO damping values were taken from Eqn. (13) with a 0.75 MN.m.s limit.

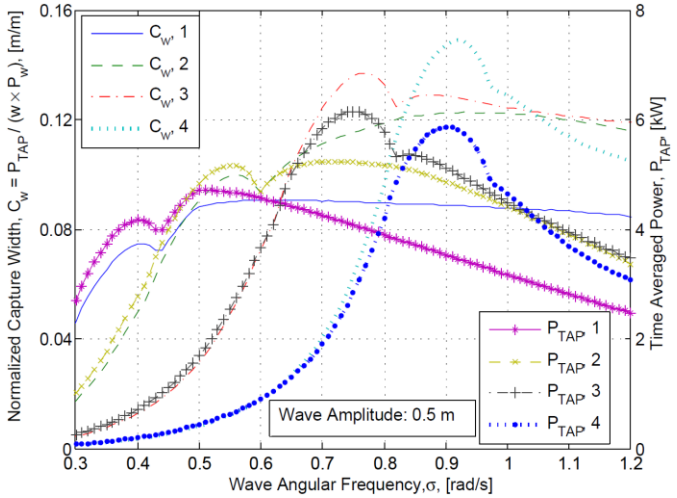

Fig. 19: Variation of time-averaged power and nondimensional capture width for four geometric configurations. PTO damping values were taken from Eqn. (13) with a 0.75 MN.m.s limit.

A. Lorentz Linearization

The frequency domain analysis used predominantly throughout this document cannot be used to model nonlinear systems; however, if the nonlinear terms can be linearized then spectral analysis in the frequency domain is still possible. For sinusoidal waves the torque generated by the nonlinear drag term can be substituted by a linear term using the Lorentz linearization [18]. This method consists of ensuring the work done over one wave cycle is the same for both linear and nonlinear expressions and can be represented by:

$$\left\langle \Lambda \dot{\theta}^2 \right\rangle = \left\langle \Lambda_{nl} \left| \dot{\theta} \right| \dot{\theta}^2 \right\rangle \quad , \tag{22}$$

where <·> stands for the average over one wave cycle, Λ is the linearized viscous damping coefficient, and Λ_{nl} is the nonlinear viscous damping coefficient. The result from integrating both terms in Eqn. (22) over one wave cycle provides the following expression for the linearized damping coefficient:

$$\Lambda = \frac{8|\xi_5|\sigma}{3\pi} \Lambda_{nl} \quad . \tag{23}$$

The linearized viscous damping coefficient can now be inserted into Eqn. (10) leading to:

$$\frac{\xi_5}{A} = \frac{X_5}{\left[C_{55} - \sigma^2 (I_{55} + \mu_{55})\right] + i\sigma \left[\lambda_{55} + B_g + \frac{8|\xi_5|\sigma\Lambda_{nl}}{3\pi} \right]} \tag{24}$$

A result of the substitution is the presence of the device amplitude of motion on both sides of the equation. An iterative-zero solver is required and the response is no longer invariant to the incoming wave amplitude. It is possible to combine Eqn. (12) and Eqn. (24), with slight modifications, to form a constrained nonlinear optimization problem. The problem can be solved using the MATLAB [19] function *fmincon* similar to the procedure described in Folley et al. [20]. As a result the PTO damping required for optimum power absorption can be quickly obtained allowing for faster design iterations rather than running lengthy time-domain simulations.

A sample set of results from solving the nonlinear problem is shown in Fig. 20–Fig. 25 comparing wave amplitudes of 0.25 and 2 m. A maximum pitch amplitude of 30 degrees was set and the PTO damping was limited to 0.75 MN.m.s. As seen in Fig. 20, the power capture efficiency is the greatest because the incoming wave amplitude is too low to reach the imposed motion constraints; thus, the body is allowed to oscillate freely. In this regime, the actuation of the foils is desired to maximize power absorption. The response of the four geometric configurations can be found in Fig. 21, in which the typical resonant motion is still observed with the four-flap configuration. The optimum PTO damping plotted in Fig. 22 shows a minimum at each resonant frequency;

This report is available at no cost from the National Renewable Energy Laboratory (NREL) at www.nrel.gov/publications.

however, as a result of the viscous damping contribution the PTO damping does not equal the wave damping.

As the wave amplitude is increased to 2 m, in certain configurations and wave conditions a feasible solution cannot be found and are not plotted in Fig. 23. As seen in Fig. 24, both the three- and four- flap configurations hug the upper limit on pitch motion because the damping magnitude is large enough to control the device. See Fig. 25; however, for the other geometries, the PTO damping cannot reduce the motion amplitude below 30 degrees. As such, it will be necessary for the geometry to open to the three-flap configuration to remain in operation and optimize power absorption. In this regime the flaps are successful at shedding hydrodynamic loads.

VIII. Conclusions

This paper has proposed a new wave energy converter device concept that has combined an OSWEC with active control surfaces. The control surfaces were shown to be effective at altering the device geometry to reduce the design loads and increase the capacity factor in larger sea states. Furthermore, the design was shown to be effective at tuning the hydrodynamic characteristics to match the resonant frequency of the device to the dominant wave-excitation frequency, which allows for optimum power extraction. The current analysis has focused purely on regular waves, while assuming the PTO provides a constant and continuous linear damping coefficient; though, it is known that active control of the PTO system can be used to further optimize power absorption.

The device concept was evaluated using traditional linear frequency domain techniques. The performance sensitivity to foil pitch angle, foil cross section, and number of activated foils were presented to describe the design evolution and highlight areas of future research. The analysis was further improved by introducing nonlinear hydrodynamics, namely, a quadratic viscous drag moment. The nonlinear model was then used to examine how performance varied with wave height. The viscous drag contribution was linearized using the Lorentz theorem, which allowed for construction of a nonlinear optimization problem that incorporated both motion and PTO constraints. The results highlighted the ability of the device to adapt to various wave climates in terms of power optimization, increased capacity factor, and reduction of hydrodynamic loads. Future work will be required to evaluate the structural and actuator requirements to determine final feasibility.

Acknowledgment

This work was supported by the U.S. Department of Energy under Contract No. DE-AC36-08GO28308 with the National Renewable Energy Laboratory. Funding for the work was provided by the DOE Office of Energy Efficiency and Renewable Energy, Wind and Water Power Technologies Office.

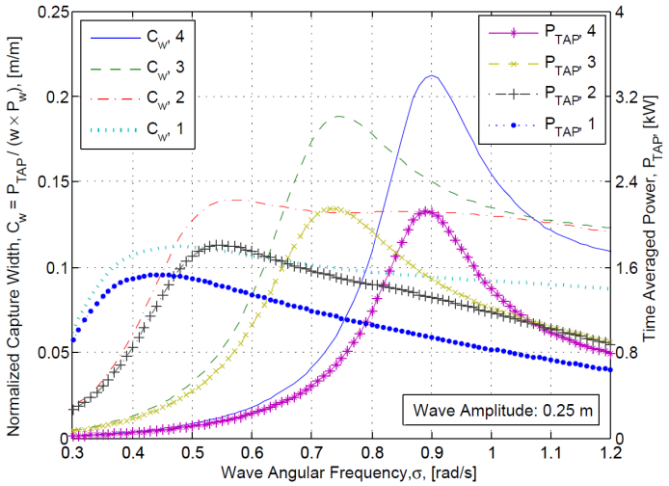

Fig. 20: Constrained time-averaged power and nondimensional capture width for four configurations using the nonlinear optimizer with A= 0.25 m.

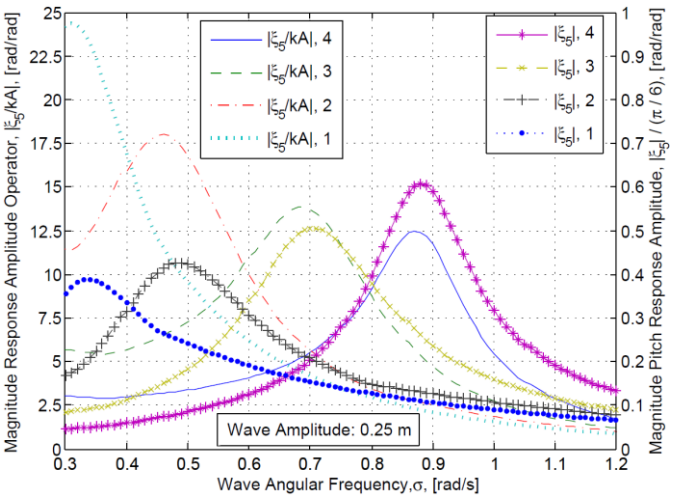

Fig. 21: Constrained RAO magnitude and pitch amplitude for four configurations using the nonlinear optimizer with A = 0.25 m.

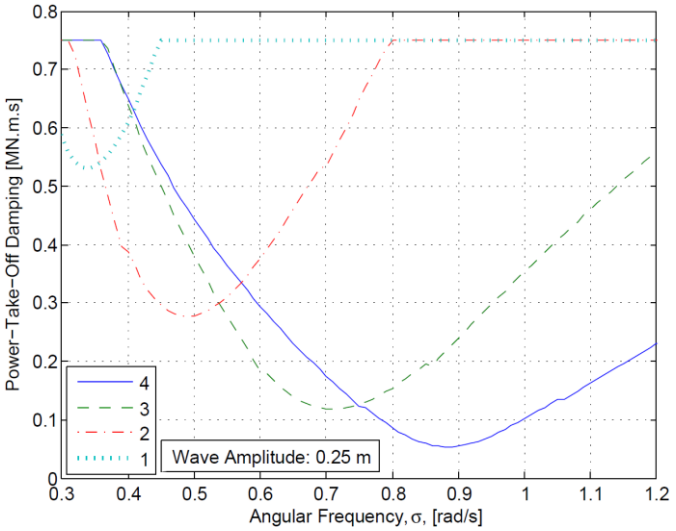

Fig. 22: Constrained optimum PTO damping for four configurations using the nonlinear optimizer with A = 0.25 m.

This report is available at no cost from the National Renewable Energy Laboratory (NREL) at www.nrel.gov/publications.

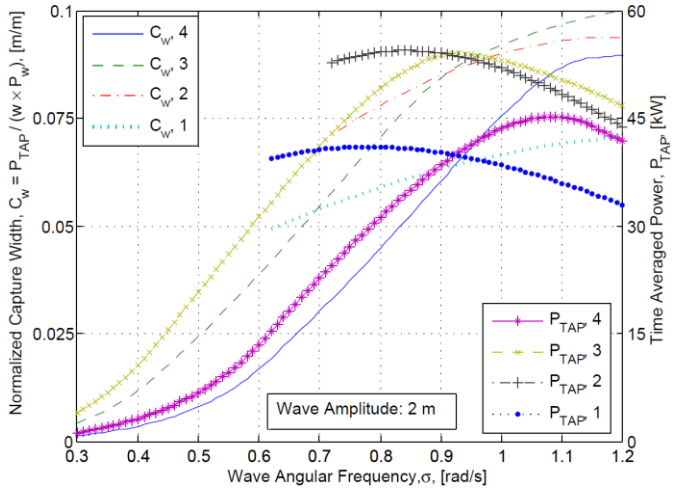

Fig. 23: Constrained time averaged power and nondimensional capture width for four configurations using the nonlinear optimizer with A = 2 m.

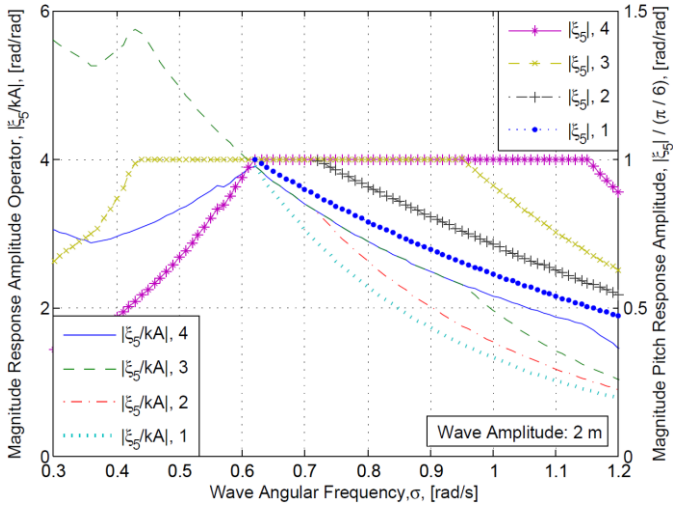

Fig. 24: Constrained RAO magnitude and pitch amplitude for four configurations using the nonlinear optimizer with A = 2 m.

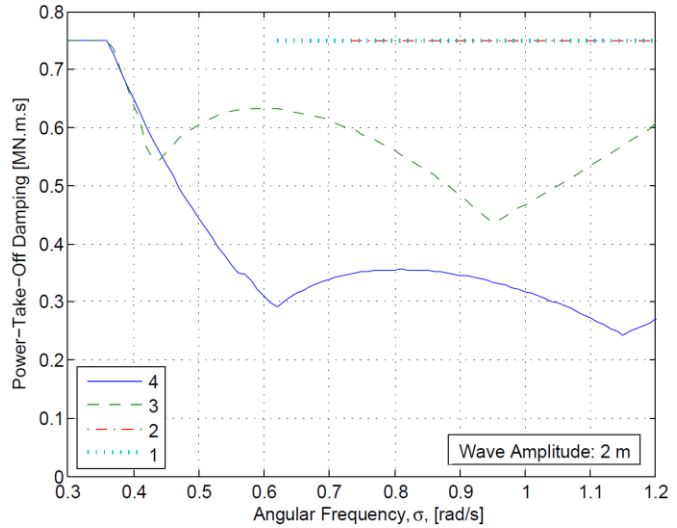

Fig. 25: Constrained optimum PTO damping for four configurations using the nonlinear optimizer with A = 2 m.

REFERENCES

[1] J. Weber, R. Costello, and J. Ringwood, "WEC Technology Performance Levels (TPLs) – Metric for Successful Development of Economic WEC Technology," in *Proc. of 10th European Wave and Tidal Energy Conference*, 2013.

[2] W. Musial, M. Lawson, and S. Rooney, "Marine Hydrokinetic Technology (MHK) Instrumentation, Measurement, and Computer Modeling Workshop," National Renewable Energy Laboratory, Golden, CO, Tech. Rep. NREL/TP-5000-57605, May 2013.

[3] S. G. Siegel, C. Fagley, M. Romer, and T. E. McLaughlin, "Experimental wave cancellation using a cycloidal wave energy converter," in *Proc. 9th European Wave and Tidal Energy Conference*, 2011.

[4] A. Kurniawan, D. Greaves, and J. Chaplin, "Wave energy devices with compressible volumes," *Proc. R. Soc. A,* vol. 470, 20140559, Oct. 2014.

[5] N. Wang, K. E. Johnson, and A. D. Wright, "Comparison of strategies for enhancing energy capture and reducing loads using LIDAR and feedforward control," *IEEE Trans. Control Syst. Technol.*, vol. 21, issue 4, pp. 1129-1142, 2013.

[6] E. Ramudu, "Ocean wave energy-driven desalination systems for off-grid coastal communities in developing countries," *IEEE Global Humanitarian Technology Conference*, Seattle, WA, Oct. 30 – Nov. 1, pp. 287-289, 2011.

[7] A. Pecher, J. Kofoed, J. Espedal, and S. Hagberg, "Results of an experimental study of the Langlee wave energy converter," *in Proc .of 20th Intl. Offshore and Polar Eng. Conf.,* Beijing China, June 20-25, pp. 877-885, 2010.

[8] P. Schmitt, S. Bourdier, D. Sarkar, E, Renzi, F. Dias, K. Doherty, T. Whittaker, and J. van't Hoff, "Hydrodynamic loading on a bottom hinged oscillating wave surge converter," *in Proc.of 22nd Intl. Offshore and Polar Eng. Conf.*, Rhodes, Greece, June 17 - 22, pp. 550 - 560, 2012.

[9] F. Flocard and T. D. Finnigan, "Increasing power capture of a wave energy device by inertia adjustment," *Applied Ocean Research*, vol. 34, pp. 126 - 134, Jan. 2012.

[10] A. J. Caska and T. D. Finnigan, "Hydrodynamic characteristics of a cylindrical bottom-pivoted wave energy absorber," *Ocean Eng.*, vol. 35, pp. 6 - 16, June 2008.

[11] D. Clabby, A. Henry, M. Folley, and T. Whittaker, "The effect of the spectral distribution of wave energy on the performance of a bottom hinged flap type wave energy converter," *in Proc. of 31st Intl. Conf. on Ocean, Offshore, and Arctic Eng.*, Rio de Janerio, Brazil, July 1 - 6, OMAE2012-83398, 2012.

[12] C. H. Lee, *WAMIT Theory Manual*, Massachusetts Institute of Technology, 1995.

[13] D. V. Evans, "A Theory for wave-power absorption by oscillating bodies," *J. Fluid Mech.*, vol. 77, issue 1, pp. 1 – 25, Sept. 1976.

[14] D. V. Evans, "Maximum wave-power absorption under motion constraints," *Appl. Ocean Res.*, vol. 3, issue 4, pp. 200 – 203, Jan. 1981.

[15] R. W. Yeung and Y. Jiang, "Effects of shaping on viscous damping and motion of heaving cylinders," *in Proc. of 30th Intl. Conf. on Ocean, Offshore, and Arctic Eng.,* Rotterdam, The Netherlands, June 19 – 24, OMAE2011-50243, 2011.

[16] J. R. Morison, J. W. Johnson, and S. A. Schaaf, "The force exerted by surface waves on piles," *J. Petroleum Technology*, vol. 2, issue 5, pp. 149 - 154, May 1950.

[17] A. Babarit, J. Hals, M. J. Muliwan, T. Moan, and J. Krokstad, "Numerical benchmarking study of a selection of wave energy converters," *Renewable Energy,* vol. 41, pp. 44 – 63, May 2012.

[18] J. T. Zimmerman, "On the Lorentz linearization of a quadratically damped forced oscillator," *Physics Letters A*, vol. 89, issue 3, pp. 123 – 124, 1982.

[19] MATLAB Release 2014a, The MathWorks, Inc., Natick, Massachusetts, United States. Retrieved from http://www.mathworks.com/products/matlab, 2014.

[20] M. Folley, T. W. Whittaker, and J. van't Hoff, "The design of small seabed-mounted bottom-hinged wave energy converters," *in Proc. 7th European Wave and Tidal Energy Conference*, Porto, Portugal, Sept. 11 – 14, pp. 1 - 10, 2007.

This report is available at no cost from the National Renewable Energy Laboratory (NREL) at www.nrel.gov/publications.